

● *Original Contribution*

SCATTERING SIGNATURES OF NORMAL VERSUS ABNORMAL LIVERS WITH SUPPORT VECTOR MACHINE CLASSIFICATION

JIHYE BAEK,^{*} SEDIGHEH S. POUL,[†] TERRI A. SWANSON,[‡] THERESA TUTHILL,[‡] and KEVIN J. PARKER^{*}

^{*} Department of Electrical and Computer Engineering, University of Rochester, Rochester, New York, USA; [†] Department of Mechanical Engineering, University of Rochester, Rochester, New York, USA; and [‡] Pfizer Inc., Cambridge, Massachusetts, USA

(Received 11 June 2020; revised 30 July 2020; in final form 6 August 2020)

Abstract—Fifty years of research on the nature of backscatter from tissues has resulted in a number of promising diagnostic parameters. We recently introduced two analyses tied directly to the biophysics of ultrasound scattering: the H-scan, based on a matched filter approach to distinguishing scattering transfer functions, and the Burr distribution for quantification of speckle patterns. Together, these analyses can produce at least five parameters that are directly linked to the mathematics of ultrasound in tissue. These have been measured *in vivo* in 35 rat livers under normal conditions and after exposure to compounds that induce inflammation, fibrosis, and steatosis in varying combinations. A classification technique, the support vector machine, is employed to determine clusters of the five parameters that are signatures of the different liver conditions. With the multiparametric measurement approach and determination of clusters, the different types of liver pathology can be discriminated with 94.6% accuracy. (E-mail: kevin.parker@rochester.edu) © 2020 World Federation for Ultrasound in Medicine & Biology. All rights reserved.

Key Words: Ultrasound scatter, Liver fibrosis, Steatosis, Inflammation, Speckle, Tissue characterization, Support vector machine, Multiparametric analysis, Principal component analysis.

INTRODUCTION

Assessment of the structural and functional state of the liver is a primary concern for diagnostic imaging (Taylor and Ros 1998; Ozturk et al. 2018). Ultrasound examination of the liver is an accessible and inexpensive tool across most of the world. There is a long and distinguished history of research in the ultrasound echoes returning from the liver, and their change with diseases, from early tissue characterization work (Chivers and Hill 1975; Gramiak et al. 1976; Bamber 1979; Lizzi et al. 1983; Campbell and Waag 1984; Insana et al. 1990; Zagzebski et al. 1993) to more recent investigations (Higuchi et al. 2014; Al-Kadi et al. 2016; Liao et al. 2016; Zhou et al. 2018; Lin et al. 2019; Tamura et al. 2020). At this point in time there are a variety of research techniques available and growing numbers of commercial scanners that offer new parameters related to echoes from tissue. Yet agreement on the precise properties of ultrasound from normal and diseased livers remains elusive. This situation is mirrored by

uncertainty as to the most appropriate physical and mathematical models of scattering from the normal and diseased tissues.

There are, however, numerous studies characterizing the diseases using ultrasound images or derived parameters (D'Souza et al. 2019); furthermore, these have been introduced into computer-aided diagnostic systems using machine learning. For example, the characterization of normal, cirrhotic and hepatocellular carcinoma has been studied (Virmani et al. 2013a, 2013b). The grade of liver fibrosis was determined by feature extraction and the support vector machine (SVM) (Yeh et al. 2003). Breast tumors were identified as benign or malignant using image processing including segmentation and feature extraction (Wu et al. 2012).

Almost all machine learning studies have employed ultrasound images as the input and used common image processing techniques including segmentation and feature extraction (Chang et al. 2010; Acharya et al. 2012). Some researchers employed parameters extracted from the images (such as contrast, signal-to-noise ratio and standard deviation) (Sujana et al. 1996; Ogawa et al. 1998).

Address correspondence to: Kevin J. Parker, University of Rochester, Computer Studies Building 724, Box 270231, Rochester, NY 14627-0231, USA. E-mail: kevin.parker@rochester.edu

Although previous studies tried to include multiple features as the input for training, the majority are based on image processing metrics, which frequently are inter-related. In general, having more independent features results in more accurate classifications. In this study, we derive independent estimates of ultrasound first- and second-order statistics based on biophysical models.

Because pathology scores are based on fatty, cirrhotic and ballooning content of the liver, we first examine the theoretical models of scattering that are likely to be dominant in cases of normal, steatotic, fibrotic, and inflamed liver tissues. Second, the effect of these scattering models on the returning echoes is examined in terms of their first-order statistics (the histogram of echo amplitudes) and second-order statistics (the backscatter vs. frequency). Third, we examine liver echoes from rat livers using a high-frequency ultrasound scanner, with and without carbon tetrachloride (CCl_4), or concanavalin A (ConA) exposure, which incites a hepatic response, including varying degrees of fat accumulation, fibrosis, and inflammation. Finally, a SVM was implemented to classify the clusters of pathologic liver states in multiparametric space.

These results provide the beginning of a coherent framework for determining the signatures or clustering in multiparametric space of the normal liver compared with steatotic, fibrotic, or inflammatory livers.

THEORY

Fractal branching theory for normal liver

The pioneering studies of ultrasound scattering from human and animal livers established a number of key results (Chivers and Hill 1975; Gramiak et al. 1976; Bamber 1979; Zagzebski et al. 1993). The frequency dependence of scattering was found to be a power law function of frequency, for example, the average intensity rising as $f^{1.4}$ power (Campbell and Waag 1984). The speckle statistics of the returning echo amplitudes were found to be somewhat analogous to that of optical speckle (Burckhardt 1978). Most of the work on scattering theory postulated scattering from spheres or spherical correlation functions, mostly attributed to cell size and shapes (Lizzi et al. 1983; Insana et al. 1990). However, more recently we postulated that scattering from the normal liver is dominated by the weak acoustic impedance mismatch between the branching fractal structure of the fluid-filled vascular bed and the surrounding parenchyma comprised of mostly close-packed hepatocytes. In this theoretical framework, the mathematics of speckle and scattering is not based on historical models of random points or spheres, but on the mathematics of scattering from cylinders and fractal branching structures (Parker 2019a, 2019b; Parker et al. 2019) as

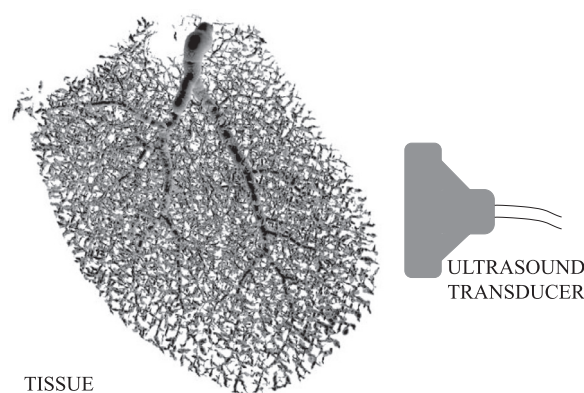


Fig. 1. Schematic of dominant scattering structures from normal liver tissue in an abdominal ultrasound scan. Shown is a micro-computed tomography contrast-enhanced 3-D rendering of the vasculature within a mouse liver. In normal liver, the weak scattering from the fluid-filled vasculature is a major source of returning echoes. Mathematical models of speckle and scattering can account for the fractal nature of the vascular tree.

illustrated in Figure 1. A key parameter in fractal analysis is the fractal dimension D , which, in 3-D structures such as the liver vasculature, is a measure of how the self-similar and multiscale elements progressively fill a 3-D volume. Measurements of fractal dimensions of vascularized tissues tend to estimate D in the range 2–2.5 (Carroll-Nellenback et al. 2020; Parker and Poul 2020b). The fractal structure's key parameters are summarized in Table 1. Furthermore, the probability distribution function for speckle amplitudes from the fractal branching vasculature are dominated by a power law relationship related to D , specifically in the form of a classic Burr distribution (Parker and Poul 2020a).

Rayleigh scattering for simple steatosis

The most elementary model for scattering from a liver with early steatosis is an *additive* model, where the base model for a normal liver still applies with the addition of the scattering from the accumulating fat. In early stages of fat accumulation in the liver, microvesicles and macrovesicles appear within hepatocytes. On pathology slides these can appear as small randomly positioned spheres ($<20 \mu\text{m}$), and because they are composed of triglycerides, these have a speed of sound and density different from those of the surrounding hepatocytes and, hence, are a source of scattering. Classic models of random Rayleigh scatterers may apply with the long-wavelength approximation of backscattered intensity increasing as f^4 power across conventional imaging frequencies. However, it may be too simple to consider only randomly positioned, single spherical scatterers as models of the inhomogeneous fat vesicles, particularly

Table 1. Interrelationship of fractal metrics in three dimensions

Name	Symbol	Equation	Notes
fractal dimension	D	$N(l) \sim l^{-D}$	box counting with scale l ; $D < 3$
autocorrelation	$C(r)$	$C(r) \sim C_0/r^{(3-D)}$	r is autocorrelation lag in spherical coordinates; $r > 0$; $D < 3$
3D spherical Fourier transform	${}^{3DS}\mathfrak{S}\{\}$	${}^{3DS}\mathfrak{S}\{1/r^{(3-D)}\} \sim 1/q^D$	q is spatial frequency; $1 < D < 3$
scattering differential cross section	$\sigma_d(k)$	$\sigma_d(k) \sim k^{(4-D)}$	k is wavenumber, derived from Fourier transform of $C(r)$; $D < 3$
speckle probability histogram	$p[A]$	$\frac{2A^{(b-1)}}{\lambda^2 \left[\left(\frac{A}{\lambda}\right)^2 + 1 \right]^b}$	$p[A]$ is the probability of an echo of amplitude A , based on scattering from a fractal branching vasculature with power law parameter b and scale factor λ , related to the classical Burr probability distribution

as the percentage of fat increases. As the steatosis progresses, the spatial distribution of fat can be heterogeneous, concentrating in periportal patterns (Schwen *et al.* 2016). Furthermore, the composition of fat in later stages can be shifted (Peng *et al.* 2015; Chiappini *et al.* 2017), so both the size distribution and the scattering strength may be a function of the stages of progression of simple steatosis. The clustering effect across a number of scales from the smallest microvesicles to the larger portal structures may mimic a fractal clustering structure (Javanaud 1989; Shapiro 1992), which then comports with the general behaviors described in Table 1.

Thin septae for CC14 fibrosis

As illustrated in Figure 2, early fibrosis response after CCl_4 exposure is in the form of thin septae that extend around the portal triads within the liver. These can be $< 20 \mu\text{m}$ in thickness and represent a sheet of increased density and compressibility compared with surrounding hepatocytes. Thus, these form a network of scattering sites which we model as additive to the baseline model for normal liver. In simplest theory, the 1-D convolution model for normal incidence on a thin sheet predicts a scattering transfer function proportional to f^{-1} (Macovski 1983; Parker 2016). This represents an upshift in the scattering amplitude transfer function compared with baseline values of $f^{0.7}$ (or $f^{1.4}$ in intensity) by Campbell and Waag (1984).

Influence of inflammation

The effects of early inflammation include the presence of ballooning of cells, necrosis and apoptosis (Lackner 2011), which could be modeled as a spherical impedance mismatch with respect to the surrounding hepatocytes, thereby serving as a source of Rayleigh scattering. This would contribute a scattering transfer function proportional to f^4 power in intensity (f^2 in amplitude) at long wavelengths. However, if the volume percent of swollen cells is low, and their Rayleigh scattering is weak, these additive contributions could be

difficult to separate out from the stronger effects of the baseline scattering, plus steatosis, plus fibrosis if present.

Influence on H-scan and Burr parameters

The theoretical scattering models listed above are hypothesized to be *additive* to the baseline case of the normal liver. In our study the particular measurements employed are related to the H-scan analysis, a matched filter approach sensitive to scattering transfer functions. In addition, the analysis of speckle amplitude histograms is studied. The details of these analyses are given under Methods, and the analyses produce five estimated parameters. Our hypothesis, based on the scattering models, is that these metrics will be sensitive to changes in the hepatic scattering structures under conditions of fibrosis, steatosis, and inflammation. The trends are given in Table 2. Briefly, under the additive models, most parameters are expected to increase with the addition of scattering structures. The exceptions are for ultrasound attenuation under fibrosis and inflammation, where the addition of low-attenuating collagen and fluid, respectively, lowers the overall loss. However, we currently lack the accurate parameters (*e.g.*, the size distribution and material properties of the fat vesicles) required for quantitative predictions. For that reason, the principal components analysis and clustering of classes using the SVM will be applied to the measured results. These are described in later sections.

METHODS

Study design and animals

An *in vivo* study was designed as illustrated in Figure 3 to investigate normal and diseased liver in rats. All animals were maintained according to the National Institutes of Health (NIH) standards established in the *Guide for the Care and Use of Laboratory Animals*. The Pfizer Animal Care and Use Committee approved all experimental protocols. Rats were pair-housed, had free access to water and were fed a standard commercial laboratory-certified rodent diet (No. 5002, PMI Feeds, Inc.). The testing facility maintained a 12-h light/dark cycle,

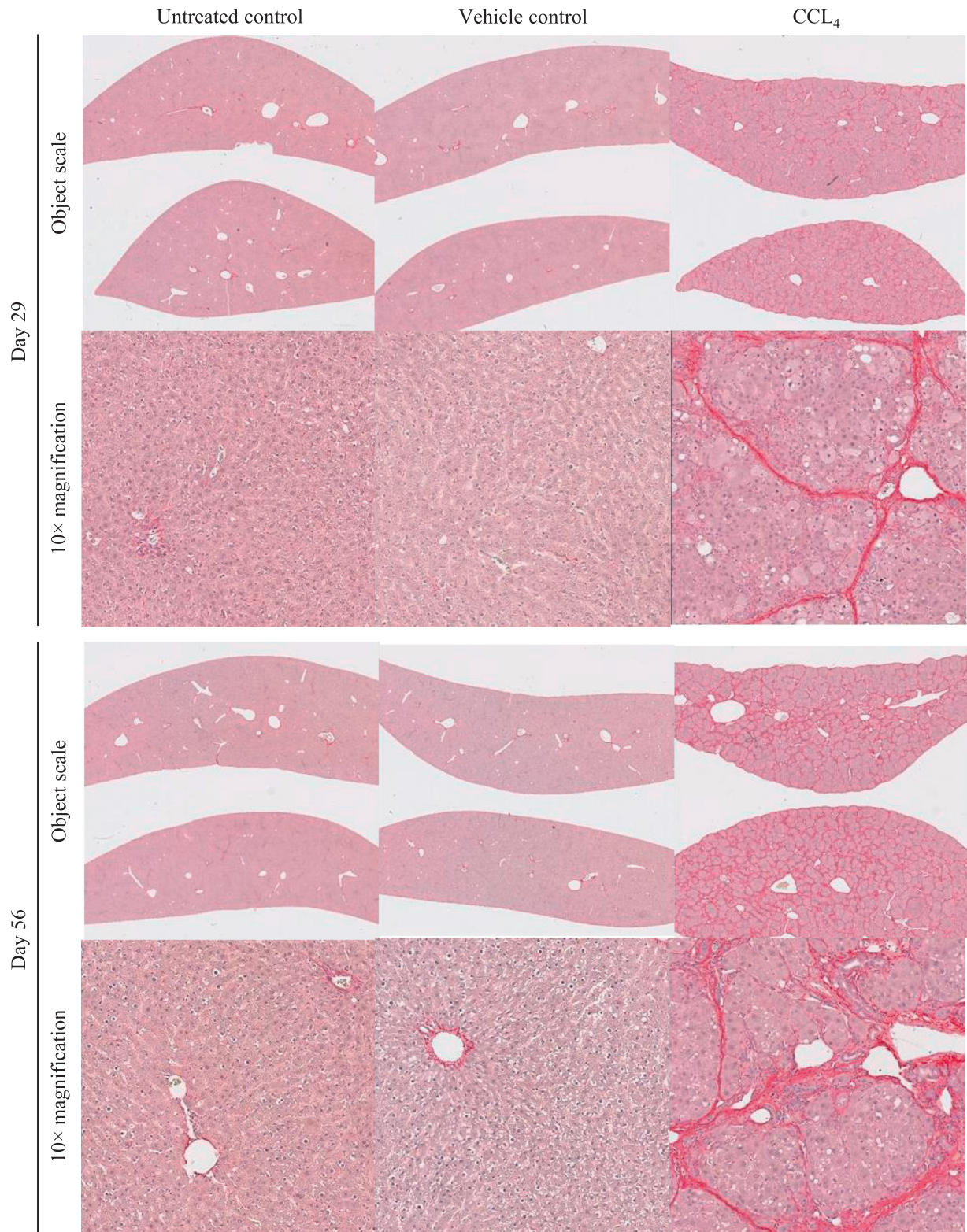


Fig. 2. Histology images of liver sections stained with picosirius red for fibrosis. Object scale and 10 × object virtual magnification are shown. Left, middle, and right columns represent untreated control, vehicle control, and fibrosis induced by CCl₄ administration; fibrosis structures were stained picosirius red and are shown in the right column images. The upper set of images denoted as “day 29” were obtained 29 d after the start of dosing CCl₄ as a fibrosis inducer; similarly, the lower set was obtained 56 d after the start of dosing. Control and vehicle groups appear to be unchanged; however, the CCl₄ dosing group in the right column exhibits fibrosis growth from days 29 to 56.

Table 2. Hypothesized changes in measured parameters based on additive models of scattering from fibrosis, fat and inflammation*

	H-Scan			Burr	
	% Blue: higher frequency scattering	α : Attenuation	I_{dB} : Brightness	b : Number density fractal branching	λ : Scale of echoes from fractal branching
Normal	50% by design	0.05 Np/cm/MHz	-15 dB measured	3 measured	350 measured
Fibrotic, low fat	↑	↓	↑	↑	↑
Fibrotic, high fat	dependent on distribution	↑	↑	↑↑	↑↑
Inflammation	weak ↑	weak ↓	weak ↑	weak ↑	weak ↑

* Arrow directions indicate increase or decrease.

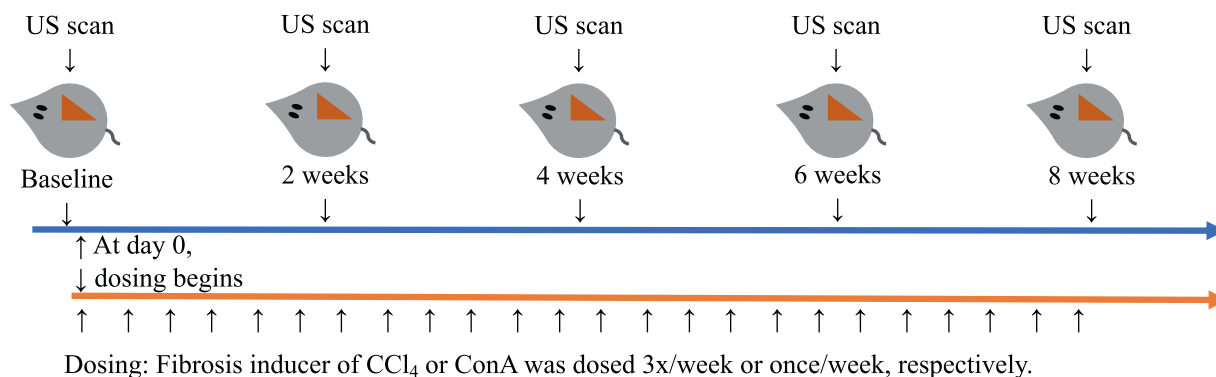


Fig. 3. Study design and data acquisition of ultrasound. All 35 enrolled rats were scanned by ultrasound every 2 wk. Twenty-six rats were dosed to induce liver diseases. At the termination of the study, rats were euthanized, and then histology and assessments were performed. ConA = concanavalin A; US = ultrasound.

with controlled temperature, humidity, and air changes. A total of 35 male rats were analyzed for this study, 31 Sprague–Dawley (SD, Charles River Laboratories, Wilmington, MA, USA) and 4 TAC NIH/RNU (nude, Taconic Biosciences, Inc., Rensselaer, NY, USA). A CCl₄ (Sigma Aldrich, St. Louis, MO, USA) model was used to induce fibrosis with varying fat, and a ConA model was used to induce inflammation. ConA has been reported to induce acute hepatitis (Heymann *et al.* 2015), and CCl₄ induces fibrosis and

varying degrees of steatosis, as outlined in Table 3. ConA was dosed intravenously once each week at a dose of 20 mL/kg in sterile phosphate-buffered saline, and CCl₄ was dosed orally three times per week (Monday, Wednesday, and Friday) at a dose of 1 mL/kg in a 1:1 mixture with the vehicle olive oil. To monitor the livers over time, rats were ultrasound imaged at baseline, that is, before dosing and every 2 wk after dosing began. A Vevo 2100 (VisualSonics, Toronto, ON, Canada) was used to image the rats

Table 3. Descriptions of the four liver groups*

Dosing	Confirmed state	Oil red O-stained area (%; mean ± SD)	No.
Control or vehicle controls (olive oil PO)	Normal	1.2 ± 1.5	9
CCl ₄	Fibrosis with low fat [†]	2.9 ± 1.9	11
CCl ₄	Fibrosis with high fat [†]	17.3 ± 11.2	6
Concanavalin	Inflammation [‡]	0.7 ± 1.6	9

SD = standard deviation.

* This study was designed to use fibrosis inducers to cause liver disease. The total of 35 rats includes 31 Sprague–Dawley and 4 nude rats, and all nude rats were confirmed as fibrotic with low fat. The four confirmed states by pathology are considered as desired classes in the support vector machine classifier. Each rat has approximately 30 ultrasound scan frames, resulting in 998 frames for training set.

[†] Fibrosis with low fat and fibrosis with high fat are classified by oil red O-stained area compared with tissue-stained area (%). Fibrosis with low fat and fibrosis with high fat have <6.5% and >9% fat, respectively.

[‡] Inflammation group has no fibrosis and very low fat, which is comparable to normal group.

with a 21-MHz center frequency linear transducer (MS 250), and radiofrequency (RF) data of the liver were collected. The liver echoes were used for signal processing to estimate tissue parameters, including H-scan classification, attenuation estimation, B-scan intensity, and ultrasound speckle statistics using the Burr distribution.

For scanning, rats were anesthetized with 1%–3% isoflurane and euthanized by CO₂ inhalation, followed by necropsy and collection of liver tissues for histology analysis. The time points for euthanasia were 4, 6, and 8 wk after dosing for 7, 12, and 16 rats, respectively. Blood serum panels were obtained at baseline and every 2 wk for liver biomarker analysis (alanine transaminase, aspartate transaminase, glutamate dehydrogenase, albumin, globulin, alkaline phosphatase, glucose, insulin, bilirubin, γ -glutamyl transferase). Fibrosis was assessed by trichrome stain and Picrosirius Red. Oil Red O stain was used to detect lipid, and the area was compared with the tissue stained area and provided a ratio (%) of oil red O stain area to tissue area as an indicator of fat content. With these measures, the liver states were categorized postmortem by an expert pathologist as described in Table 3.

H-Scan analysis

A summary of the H-scan method is given in this section; additional details can be found in Parker and Baek (2020). Fundamentally, the H-scan is a matched filter analysis that models the pulse-echo phenomenon as a power law transfer function in the frequency domain. In general, smaller structures have higher power law transfer functions, and these are encoded as *blue* on the visual display of the H-scan output. However, frequency-dependent attenuation effects can accumulate over depth and require compensation if an accurate analysis is required.

Attenuation estimation and correction within the H-scan analysis

Ultrasound imaging systems commonly employ a pulse with a round-trip impulse response that can be approximated by a bandpass Gaussian spectrum of $e^{-(f-f_0)^2/2\sigma^2}$ with a center or transmit frequency of f_0 and a bandwidth of σ . When considering the frequency and depth-dependent attenuation of $e^{-\alpha f x}$, the frequency spectrum is described by

$$S(f) = e^{-\frac{(f-f_0)^2}{2\sigma^2}} \cdot e^{-\alpha f x} \quad (1)$$

where α is the attenuation coefficient (in Np/cm/MHz), f is frequency of ultrasound (in MHz) and x is depth (in cm). The attenuation makes the peak frequency of the spectrum decrease, which can be estimated by taking the

first partial derivative with respect to f and finding 0 at peak frequency f_p given by

$$\left. \frac{\partial S}{\partial f} \right|_{f=f_p} = \left(\frac{f_p - f_0}{\sigma^2} + \alpha x \right) \cdot S(f_p) = 0. \quad (2)$$

We obtain the attenuation coefficient in the form

$$\hat{\alpha}(x) = -\frac{f_p(x) - f_0}{x \cdot \sigma^2} \quad (3)$$

where f_0 and σ represent properties of the transducer related to transmit frequency and designed bandwidth, respectively. Therefore, by measuring peak frequency along with depth of $f_p(x)$, the attenuation coefficient can be estimated according to eqn (3). This approach assumes homogeneous (or stationary) distribution of scatterers within the region of interest (ROI), but has the advantage of being independent of amplitude fluctuations related to system gain.

As an example of this approach, Figure 4a is a B-scan of a rat liver with a ROI for H-scan processing, and Figure 4b is an H-scan colormap. By averaging the color values over all scanlines within the ROI, representative H-scan color levels along with depth x can be calculated as illustrated in Figure 4 (c, d); the color levels can be converted into peak frequencies in Figure 4f by pseudocolor given in Figure 4e. The color levels from 1 to 256 are mapped to frequencies ranging from 8.7–20.3 MHz. The measured peak frequency in Figure 4f is used to estimate the attenuation coefficient in eqn (3), and the attenuation coefficients obtained are averaged over depth. In summary, the attenuation coefficient can be obtained using H-scan results within assumptions of a Gaussian bandpass pulse and attenuation of the form $e^{-\alpha f x}$.

Once the attenuation parameter is estimated for a given ROI in the liver, a depth-dependent inverse filter can be applied to correct for losses, at least to the limit of the noise floor (Parker and Baek 2020), and proceed with the matched filter analysis. The final outputs for each liver ROI are estimates of attenuation (α in dB/cm-MHz), echogenicity or brightness (dB), and percentage of blue. The attenuation coefficient was estimated by averaging eqn (3) over depth within the ROI. Brightness was calculated from log-compressed data where 0 dB is set to the same brightness level for all scans. When calculating percentage of blue, color levels obtained from H-scan ranging from 1 to 256 as illustrated in the color bar in Figure 4b were used; the pixels with color levels of [1, 128] and [129, 256] are red ($i \in R$) and blue pixels ($i \in B$), respectively. Data normalization was performed by converting the color levels from 1 to 256 into the normalized color levels I from -1 to 1 in sequence; then percentage of blue is defined by

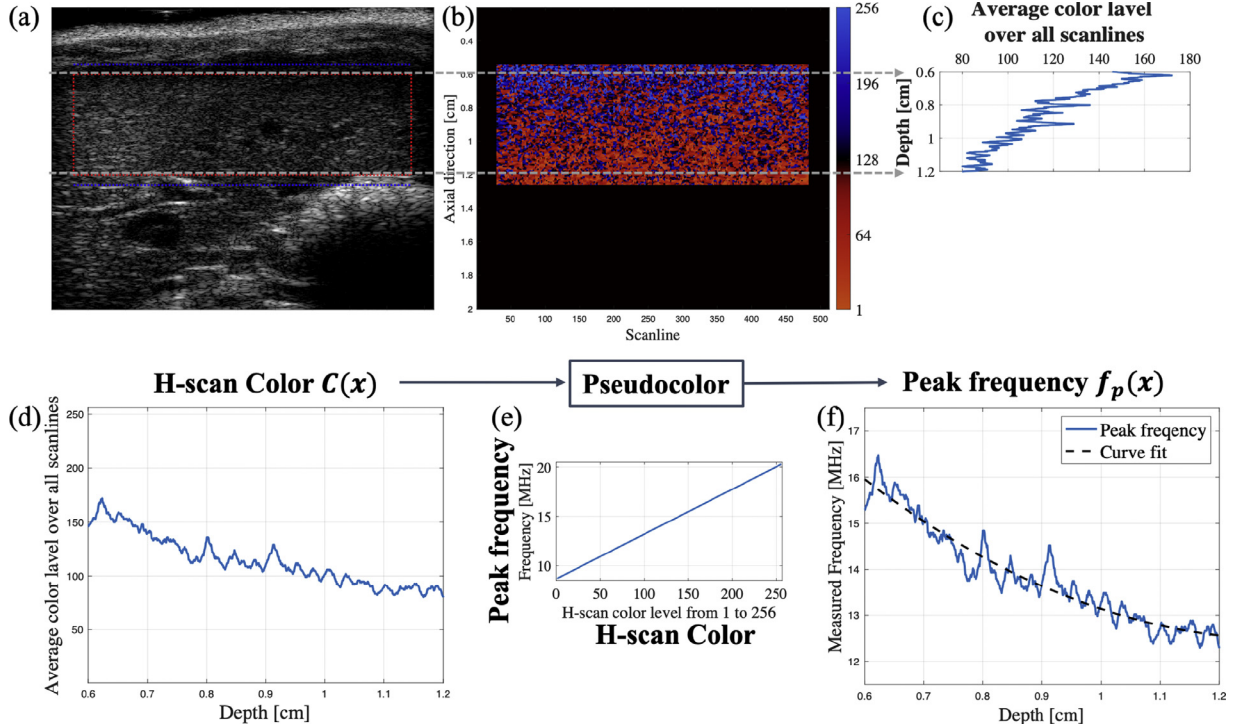


Fig. 4. Attenuation estimation using H-scan.

$$\% \text{ of blue} = \frac{\frac{1}{n_B} \sum_{i \in B} |I_i|}{\frac{1}{n_B} \sum_{i \in B} |I_i| + \frac{1}{n_R} \sum_{i \in R} |I_i|} \times 100\% \quad (4)$$

where i is the index of each pixel in B-scan, I_i is normalized color level value for the pixel i , and n_B and n_R are the numbers of blue and red pixels, respectively.

First-order statistics of speckle and the Burr distribution

Consistent with the framework provided in Figure 1 and Table 1, the normal liver's speckle pattern results from the fractal self-similar network of fluid vessels (Parker 2019b; Parker *et al.* 2019; Parker and Poul 2020a). Our analysis assumes that a broadband pulse interacts with a fluid-filled, branching, self-similar set of long vessels in the tissue, whose number density as a function of radius a is described by a power-law behavior as $N(a) = N_0/a^b$, with the key power law parameter b governing the branching behavior of the vasculature over a wide range of scales. By finding the dominant echoes from the 3-D convolution model, the histogram of echo amplitude is derived and, after normalization, can be expressed as a probability density function (PDF):

$$N_n[A] = \frac{2A(a_{\min})^{b-1}(b-1)}{A_0^2 \left[\left(\frac{A}{A_0} \right)^2 + a_{\min} \right]^b} \quad (5)$$

Equation (5) is a three-parameter PDF describing the distribution of the echo amplitude A with A_0 and a_{\min} related to the system gain and minimum size of scattering vessels, respectively. This equation reduces to a two-parameter PDF by change of variables as $\lambda = A_0 \sqrt{a_{\min}}$:

$$N_n[A] = \frac{2A(b-1)}{\lambda^2 \left[\left(\frac{A}{\lambda} \right)^2 + 1 \right]^b} \quad (6)$$

The two-parameter PDF of eqn (6) happens to be a Burr type XII distribution, which was derived in the 1940s without any consideration of ultrasound (Burr 1942). The speckle distribution has also been found to be in reasonable consistency with the parameters of the Lomax distribution when fitted to the intensity of echoes and also with the logistic distribution parameters when fitted to the natural log of echo amplitudes, by employing the general transformation principle (Parker and Poul 2020a).

The two parameters of b and λ may be sensitive to the change in the scattering structures of soft tissues. The two parameters of the Burr distribution are estimated using MATLAB's (The MathWorks, Inc., Natick, MA, USA) non-linear least-squares minimization of errors when fitted to the normalized distribution of the speckle amplitude data from the liver ROIs. To place a reasonable bound on the parameters of b and λ in curve fitting, an additional step is

taken. We calculate the mode and median of the speckle histogram and compare these with the theoretical formulas for the Burr distribution:

$$\text{Mode} = \left(\frac{1}{2b-1} \right)^{\frac{1}{2}} \cdot (\lambda) \quad (7)$$

$$\text{Median} = \left(2^{\left(\frac{1}{b-1}\right)} - 1 \right)^{\frac{1}{2}} \cdot (\lambda) \quad (8)$$

By use of eqns (7) and (8) for the mode and median of the Burr distribution, which both depend on b and λ , a system of equations is solved for each image frame's ROI to obtain frame-by-frame estimates for these two parameters. These data are used as bounds with $\pm 10\%$ to $\pm 20\%$ intervals for the histogram Burr fitting estimation of b and λ . This additional step ensures that the parameters lie in a trimmed, middle range. This process is done for all the frames for each of the selected 35 liver data and the results of the b and λ parameters presented as boxplots, separating the sensitivity of parameters in four groups of rat livers.

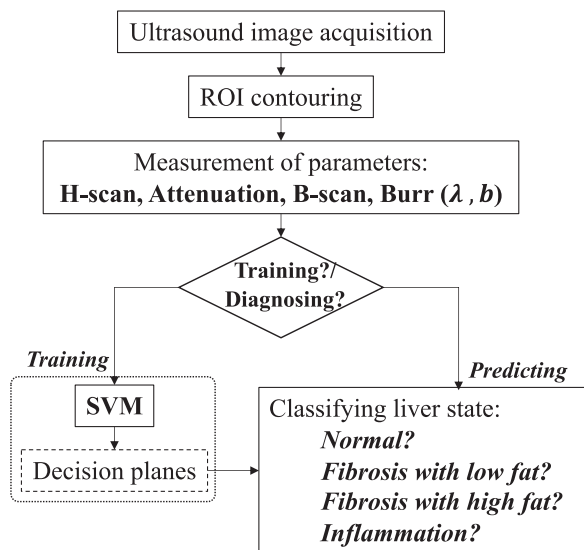


Fig. 5. Overall block diagram for support vector machine (SVM) classifier to train and predict liver states. Ultrasound scan of liver area where region of interest (ROI) is contoured. Five measurements are obtained by H-scan analysis, attenuation estimation, B-scan intensity estimation, and Burr histogram analysis with two parameters. Thus, each input image has five features that are assigned as the input of the SVM classifier. During training with a train set, SVM constructs decision planes for the four groups: normal, fibrosis with low fat, fibrosis with high fat, and inflammation. To visualize the training set and decided hyperplanes in the 3-D plane, principal component analysis was performed to reduce the number of features from five to three.

SVM classifier

The classification of liver pathology states was performed by the SVM, which results in decision planes for the classification in the 5-D parameter space: H-scan, attenuation, B-scan, and Burr b and λ . Figure 5 is a schematic of the proposed classifier. For each of the 35 rats scanned, the liver ROIs were manually set to select relatively uniform liver appearance with an absence of artifacts such as shadowing and reverberations. Each case has approximately 30 frames, including the liver; therefore, a total of 998 ultrasound images were enrolled as a training set. Instead of using the images directly as the machine learning input, this study uses the five measurements within the ROIs as the input: the percentage of blue from the H-scan, the attenuation coefficient α (dB/MHz/cm), the intensity I_{dB} (dB) from the B-scan, and λ and b (dimensionless) from Burr histogram analysis. In other words, the five measurements define the five input features of the machine learning procedure, and the total number of features is 998:

$$\left\{ \left(x^{(n)}, y^{(n)} \right) \right\}_{N=1}^{N=998}, \text{ where } x^{(n)} = (\% \text{ of blue}, \alpha, I_{dB}, \lambda, b) \in \mathbb{R}^5 \quad (9)$$

Here $y^{(n)}$ is a desired class confirmed post-mortem pathology, and there are four classes: normal, fibrosis with low fat, fibrosis with high fat, and inflammation. Ideally, the five metrics for each class form clusters in the 5-D space, whereby the goal of this machine learning study is constructing decision planes to distinguish the liver states based on the parameters. Further details of our implementation, including the training protocol, are found in the Supplementary Data, Appendix A (online only).

RESULTS

B-Scan, H-scan and attenuation parameters

The enrolled 35 rats were scanned every 2 wk, and we attempted to contour the ROIs consistently over time by using vessels or skin layer as landmarks, whereby the ROIs for the same rat are located in the relatively same position near the biomarkers over time. The selected B-scan and H-scan results are in Figure 6; ROIs for the processing are indicated using the red boxes. The H-scan of low fat fibrosis and inflammation classes appear more blue than those of normal livers, but high fat fibrosis cases show more red compared with normal cases. Selected histology results are illustrated in Figure 2, and fibrosis structures were stained in red. CCl₄-exposed rats had an increase in fibrosis from 29 to 56 d after the start of dosing, while untreated and vehicle controls remain

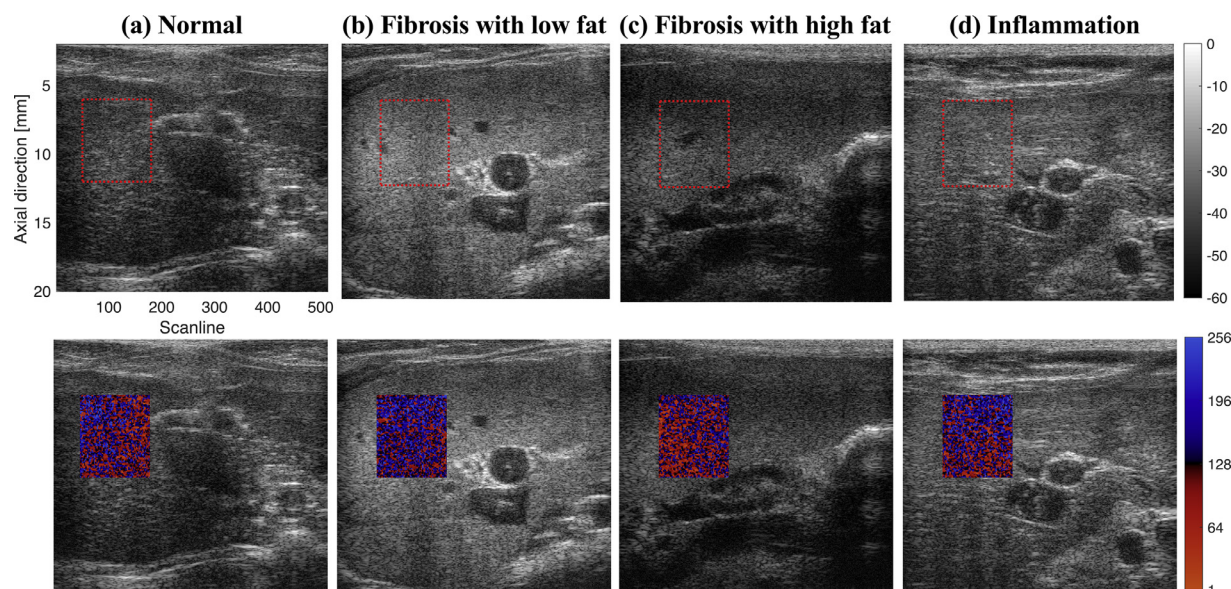


Fig. 6. B-Scan (top row) and H-scan (bottom row) images of (a) normal, (b) fibrosis with low fat, (c) fibrosis with high fat, and (d) inflammation.

unchanged over time. The thin fibrotic septae seem to divide the sinusoids, driving the H-scan results for fibrosis cases with more blue colors, indicating the addition of relatively small scattering sites.

The investigation over time and the statistical plots are provided in Figure 7. H-Scan results of low fat fibrosis and inflammation in Figure 7 (a, b) indicate an increase in percentage of blue over time, and low fat fibrosis has a greater percentage of blue than inflammation, which is also illustrated in Figure 6; low fat fibrosis in Figure 6b exhibits a greater increase in blue than the case of inflammation in Figure 6d. As for the high fat fibrosis group in Figure 7a, the effect of fibrosis growth is likely to mainly appear from the first until the fourth week as the increase in percentage of blue; but the fat accumulation effect appears later in the sixth and eighth weeks, exhibiting the decrease in percentage of blue. According to statistics in Figure 7b, the H-scan can distinguish the four groups from each other, although there are overlapped distributions between the groups. Figure 7 (c, d) represent the results of attenuation estimation. Attenuation for normal and inflammation groups remains unchanged over time. However, attenuation for fibrosis with low fat decreases over time. Attenuation for fibrosis with high fat tends to decrease until the sixth week but increase later, suggesting that the dominant effects of fat appear later, which is consistent with the H-scan trend for fibrosis with high fat. According to statistics of attenuation results in Figure 7d, attenuation can separate the four groups except for one case of comparison: normal versus high fat fibrosis. Figure 7 (e, f) illustrate the results of the B-scan. Fibrosis increases in

brightness over time, while normal and inflamed liver remain unchanged. According to the brightness of the B-scan in Figure 7f, there can be significant differences when comparing the four groups. Although normal liver and inflammation overlap, the B-scan can statistically separate the two groups; however, the B-scan indicates better separation between normal liver and fibrosis. According to the data distribution in half-violin plots in Figure 7 (b, d, and f), the three analyses play essential roles to separate some cases from others but they work well for different separations. To be specific, the B-scan indicates better separation between normal and fibrosis, although it has more overlap between fibrosis with low and high fat; however, the H-scan and attenuation can differentiate low and high fat. Furthermore, the H-scan is the method that can indicate the best separation between normal and inflammation. Therefore, combining the results can provide the potential to discriminate each case from the others.

Burr parameters

For each image frame from the 35 rat livers of this study, the analysis is performed on a well-defined ROI and the underlying Burr statistical properties of the liver speckle are derived from the envelope of the RF signal. The ROIs for the Burr study are located in the same region as those used in the H-scan and attenuation studies in this work to ensure that the analyses are applied consistently. Because of the sensitivity of the Burr parameters to the presence of large inhomogeneous regions, the ROIs were adjusted slightly if necessary to

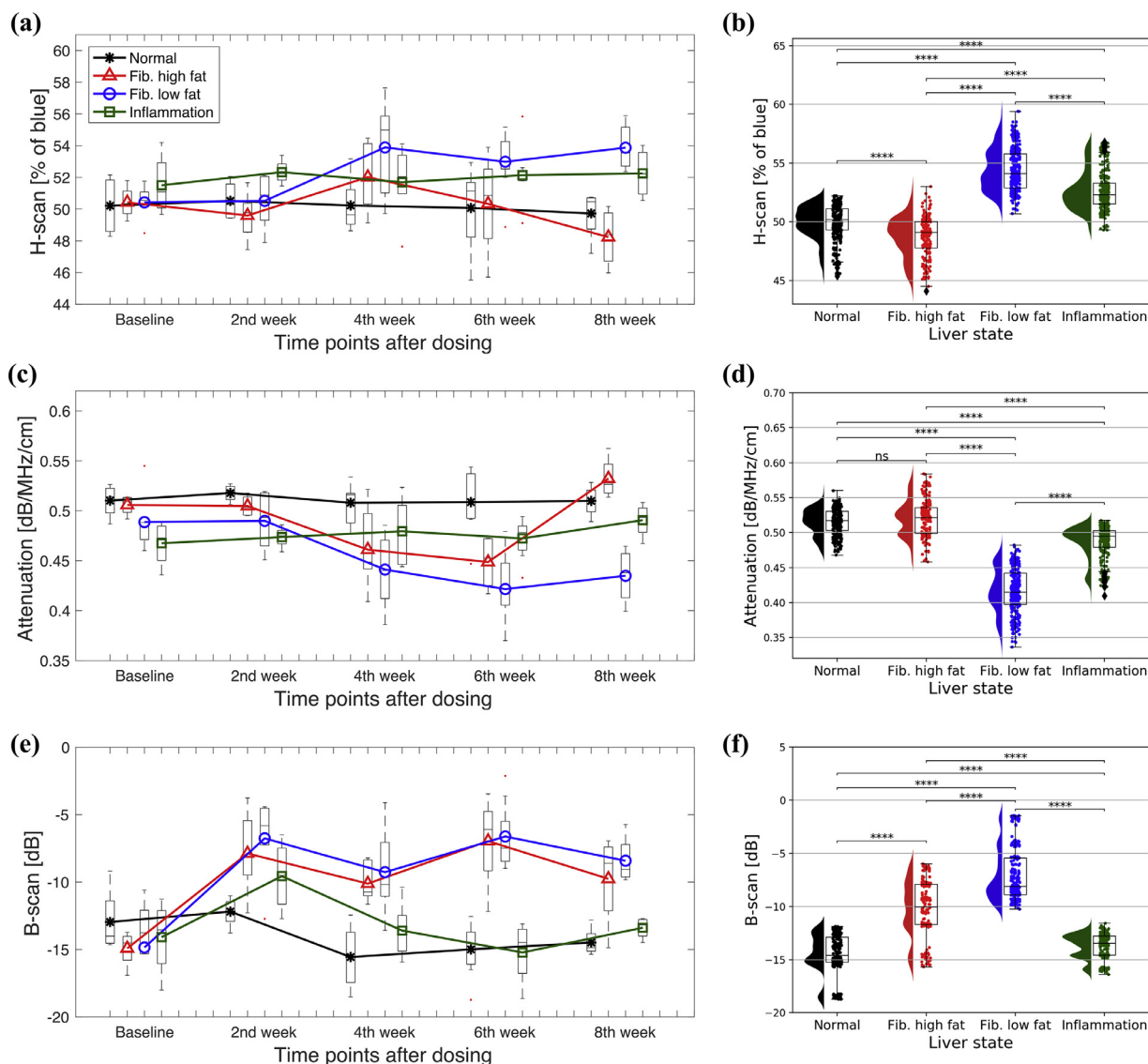


Fig. 7. H-Scan, attenuation, and B-scan result plots. Left column: Investigation over time, including progression of diseases. Right column: Statistics at the final time points for 35 rats; rats were euthanized at different time points ranging from 4 to 8 wk after the start of dosing. The following notations are used for the statistics: ns (no significance), $p > 0.05$; *, $p < 0.05$; **, $p < 0.01$; ***, $p < 0.001$; and ****, $p < 0.0001$.

avoid any major vessel or area including large nodules and artifacts.

In Figure 8 are the B-scan with the selected ROI and the histogram of normalized echo amplitude, back-scattered from speckles, fitted to the Burr distribution for one sample frame of a rat liver representing each of four groups. The corresponding b and λ parameters of the Burr distribution for each case are presented along with the results of fitting goodness as R^2 and root mean square error in Table 4. The plots of histogram of amplitudes in all four groups indicate that the Burr model gives a close fit of the pathology of liver tissues in normal liver,

fibrosis with low fat, fibrosis with high fat, and also inflammation conditions. Also, the b and λ parameters are found to be sensitive to changes in pathologic conditions of the liver. The clear trend is increasing in b and λ when the rat liver condition shifts from normal to abnormal conditions because of fibrosis, fat increase (steatosis), or inflammation. To go into more detail, b and λ increase with the presence of a high stage of fibrosis and also with increase in fat inclusion.

To summarize the results of all the analyses for the 35 rat livers considering the parameter estimates for all the frames for each rat liver, the results are shown as two

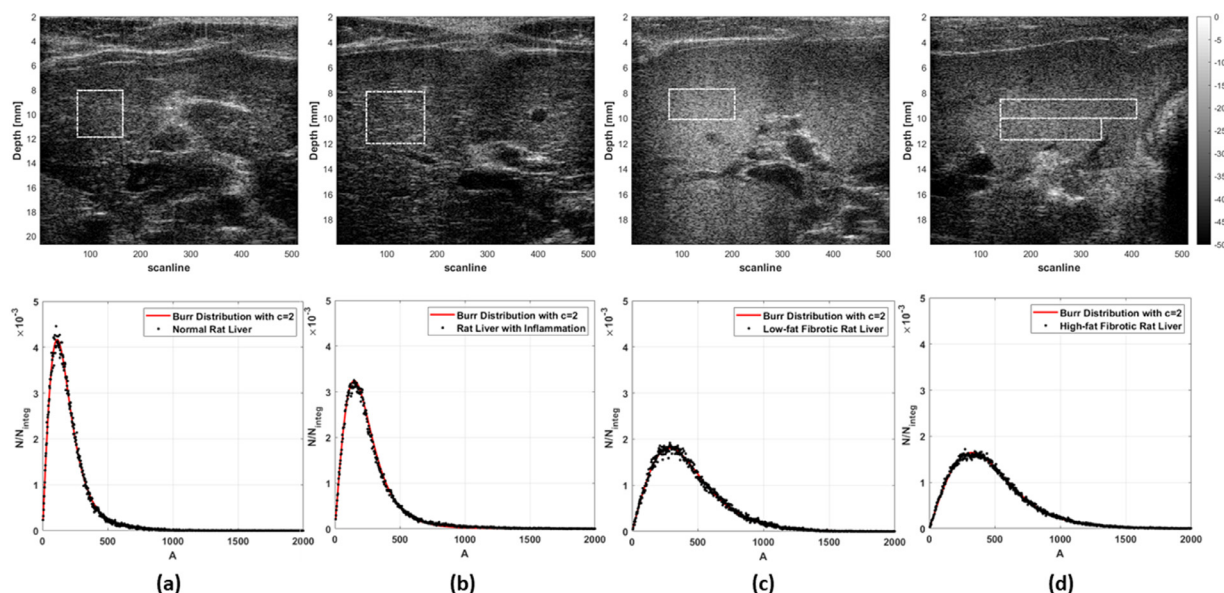


Fig. 8. Top row: B-scan image. Bottom row: Burr-fitting to the histogram of normalized echo amplitude for (a) normal rat liver, (b) rat liver with inflammation, (c) low-fat fibrotic rat liver and (d) high-fat fibrotic rat liver. The selected ROIs for Burr analysis are shown as *dashed boxes*.

separate half-violin plots in Figure 9 (a, b) for b and λ , respectively. The median of the results in each group is marked as a *horizontal line in the box* and the variation outside the quartiles appears as *dashed whiskers*. The significance of the difference between each pair was analyzed by the p value from the one-way analysis of variance and the multiple comparison test. The p value is indicated by asterisk as in Figure 7. Comparing different groups on the boxplots in Figure 9, we observe that the power law parameter b distinguishes between the four groups of rat livers, with the high-fat fibrotic group having higher values of b than the low-fat fibrotic group, and both groups show significant increases in b in comparison to the normal and inflamed liver groups. On the other hand, when looking at the λ results, the same trend is observed and the λ parameter can discriminate five of six pairs; however, the difference is less obvious because of the presence of a few outliers in the low-fat and high-fat fibrotic groups. One of the rats in the low-fat fibrotic

Table 4. Burr-fitting parameters of a rat liver sample from each of four groups along with the goodness-of-fit parameters

Dosing	b	λ	R^2	RMSE
Normal	3.06	253	0.997	0.051
Liver with inflammation	3.40	358	0.997	0.043
Low-fat fibrotic	4.60	804	0.995	0.004
High-fat fibrotic	5.41	1013	0.997	0.003

RMSE = root mean square error.

group has unusually high values of λ in comparison to the other rats in this group. This specific case produced most of the elevated outliers in Figure 9b. On histology of this case, a hemorrhage in its lung was noted, and this might be an indication of additional complications.

SVM-based classifier

The SVM-based liver state classifier was implemented, as described in more detail in the Supplementary Data, Appendix B (online only). To build the classifier, the two parameters of box constraint (C) and σ were decided according to the accuracy and shape of hyperplanes; we found that optimal values of C and σ are approximately 50 and 0.7, respectively. The final results with a classification accuracy of 94.6% is provided in Figure 10. The details of the SVM optimization procedure are further examined in the Supplementary Data, Appendix B.

To visually examine the hyperplane shapes or clusters of data set, reduced dimensions were considered as the employed features have five dimensions that cannot be visualized in 3-D space. The five dimensions were reduced to two or three dimensions using principal component analysis (PCA), as depicted in Figures 10 (c, d). To derive the principal component analysis, a uniform scaling was performed by modifying min–max normalization features (Han *et al.* 2011). Further details of this normalization and analysis are provided in the Supplementary Data, Appendix C (online only).

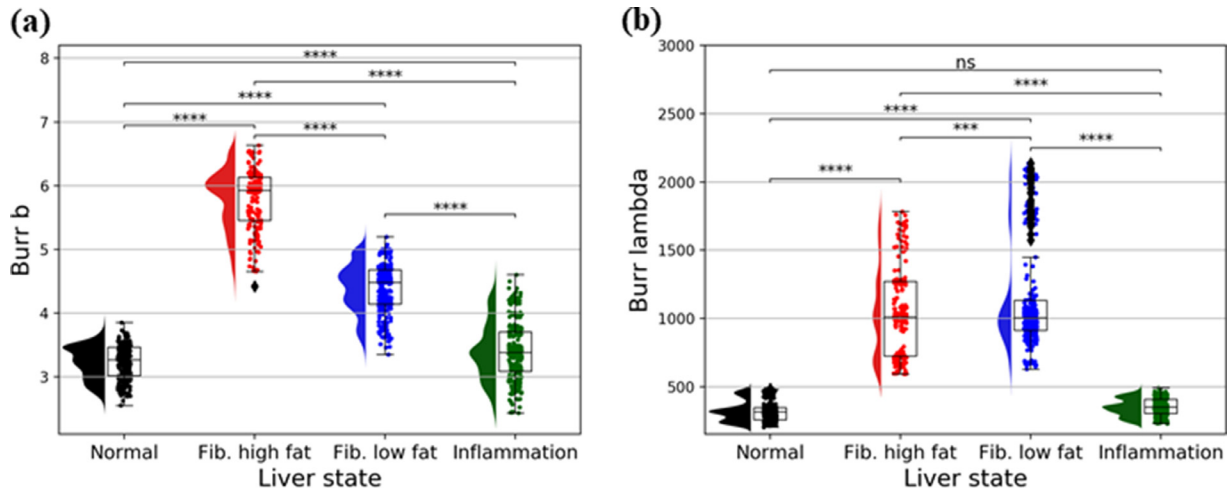


Fig. 9. Summary of Burr parameter estimation results for 35 different rat livers. (a) Boxplot of the power law parameter b . (b) the Boxplot of λ for four groups of livers. *Statistically significant difference. ns indicates that the difference is not statistically significant. The following notations are used for the statistics: ns (no significance), $p > 0.05$; *, $p < 0.05$; **, $p < 0.01$; ***, $p < 0.001$; and ****, $p < 0.0001$.

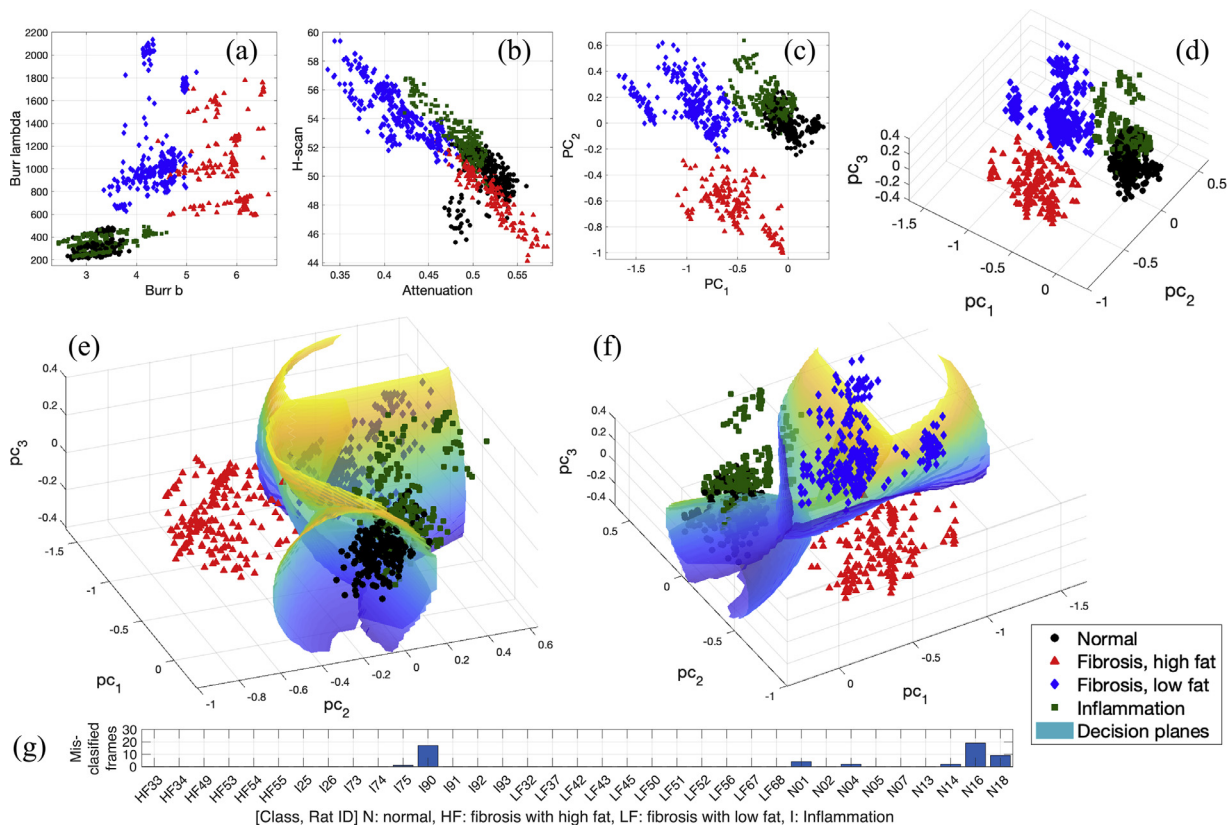


Fig. 10. View of clusters and SVM classification. (a–c) Groups in 2-D parameter space: (a) results of Burr analysis; (b) H-scan and attenuation measures. (c, d) First two and three principal components (PC) derived from the five-parameter analysis: Burr λ and b , H-scan, attenuation, and intensity. (e, f) Hyperplanes to separate the liver states in 3-D principal component space defined by the support vector machine (SVM)-based liver state classifier that were optimized and implemented in this work. (g) Misclassified cases. Classification accuracy is 94.6% for the implemented SVM-based liver classifier of this work. All fibrosis and fatty cases were correctly classified. Two cases of inflammation and five normal cases have misclassified frames. Each liver scan has approximately 30 frames.

DISCUSSION

Our SVM with the optimized parameters classified 998 image frames with the extracted five scaled features, whereby the decision planes that define liver states were produced with 94.6% classification accuracy. Figure 10g illustrates the misclassified cases among 998 data; there are a total of 35 rats, and each rat has approximately 30 frames. Although 2 and 5 rats in the inflammation and normal groups have misclassified frames, some frames were misclassified, but the others were correctly classified; for example, rat 1 in the normal group has 4 misclassified frames, but 26 frames are correctly classified. In accordance with SVM theory, our SVM classifier allows a small percentage of misclassified training data, resulting in smoother decision boundaries while avoiding overfitting. As illustrated in Figure B.1 (c, d), we can design an SVM classifier with 100% accuracy, but that would work only for the input of this study. Because the purpose of this work is to propose a liver state classifier for any liver, we have optimized the classifier at 94.6% accuracy without overfitting to reach 100% accuracy.

To visualize the clusters of the input data and classification with decision boundaries, PCA reduced the measured five features into two or three parameters because five dimensions cannot be displayed. Therefore, Figure 10 is a view of clusters with hyperplanes, which have a loss of information compared with the five-dimensional analysis mentioned in previous sections. When using only the two and three components in Figure 10 (c, d), classification accuracies of SVM are 90.5% and 91.9%, respectively; these are lower than the 94.6% accuracy of 5-D analysis because of the information loss by PCA. The reduced parameters help us to visualize the real 5-D results, but are not sufficient by themselves for the highest accuracy.

In Figure 10 (a, b) are clusters derived by scattering models related to the histogram analysis of echo amplitudes and frequency analysis, respectively: (a) Burr parameters; (b) H-scan and attenuation. Figure 10a illustrates that we can visually separate this space into three regions of normal/inflammation, low-fat fibrosis, and high-fat fibrosis with a distinctive area. It is noted that the inflammation and normal groups seem to have considerable overlap regions when applying only the two-parameter Burr analysis. Although these two are not well separable visually in Figure 10a, frequency-dependent studies of H-scan and attenuation estimation in Figure 10b can provide better separation between normal and inflammation data. Moreover, Figure 10b tends to show four separable clusters with mild overlaps. Figure 10a tends to more clearly distinguish fibrosis from normal cases than frequency analysis and Figure 10b is more likely to discriminate each case from

the other groups, combining the results can take advantage of the different methods and compensate for their drawbacks; furthermore, the conventional B-scan intensity is also added as a feature. By including all five measurements, Figure 10c illustrates clusters in reduced 2-D space generated by PCA. As expected, Figure 10 (a–c) illustrates better separation between liver state groups compared with Figure 10a or Figure 10b alone. Furthermore, when considering the first three principal components in Figure 10d, each cluster is better distinguished from the other clusters compared with 2-D space, because the first principal components have 97.7% information from the raw data, but two first principal components have 93.5%. Therefore, it is expected that use of all information on the raw data can have better discrimination than the view of clusters that is visualized in Figure 10. The decision boundaries in Figure 10 (e, f) were defined by information from the first three principal components, with 91.9% classification accuracy. However, the hyperplanes used to classify the liver states in 5-D space have 94.6% accuracy, whereby these provide better separation between liver states than 3-D space; among 998 frames investigated, the founded frames in the bar graph in Figure 10g are the only misclassified frames.

In summary, each measurement has its distinct role in distinguishing specific liver states. SVM plays a prominent role in effectively integrating the five different analyses into a combined classification. Consequently, SVM indicates that there exist the boundaries that can separate the liver states with 94.6% accuracy, meaning that each group has distinct quantitative characteristics based on the five measurements of this work.

CONCLUSIONS

In this study of an animal liver model in normal and abnormal states, we employed two relatively new analyses, the H-scan and the Burr distribution approaches. These produced five output parameters linked to ultrasound propagation and scattering models from physics. The parameters were sensitive to changes in liver structures and formed clusters in 5-D spaces that enabled a robust classification of individual livers into the diagnostic categories of normal, fibrosis (low fat), fibrosis (high fat) and inflammation. A SVM classification approach was capable of discriminating between groups with 94.6% accuracy. We believe that this supports the general argument that matching measures to biophysical models of tissues provides the strongest ability to discriminate and classify pathologic conditions.

Acknowledgments—This work was supported by National Institutes of Health Grant R21 EB025290 and by Pfizer Inc.

Conflicts of interest—The authors declare that they have no conflict of interests.

SUPPLEMENTARY MATERIALS

Supplementary material associated with this article can be found in the online version at doi:[10.1016/j.ultrasmedbio.2020.08.009](https://doi.org/10.1016/j.ultrasmedbio.2020.08.009).

REFERENCES

- Acharya UR, Vinitha Sree S, Krishnan MM, Molinari F, Garberoglio R, Suri JS. Non-invasive automated 3 D thyroid lesion classification in ultrasound: A class of ThyroScan systems. *Ultrasonics* 2012;52:508–520.
- Al-Kadi OS, Chung DYF, Coussios CC, Noble JA. Heterogeneous tissue characterization using ultrasound: A comparison of fractal analysis backscatter models on liver tumors. *Ultrasound Med Biol* 2016;42:1612–1626.
- Bamber JC. Theoretical modelling of the acoustic scattering structure of human liver. *Acoust Lett* 1979;3:114–119.
- Burckhardt CB. Speckle in ultrasound B-mode scans. *IEEE Trans Sonics Ultrason* 1978;25:1–6.
- Burr IW. Cumulative frequency functions. *Ann Math Stat* 1942;13:215–232.
- Campbell JA, Waag RC. Measurements of calf liver ultrasonic differential and total scattering cross sections. *J Acoust Soc Am* 1984;75:603–611.
- Carroll-Nellenback JJ, White RJ, Wood RW, Parker KJ. Liver backscatter and the hepatic vasculature's autocorrelation function. *Acoustics* 2020;2:3–12.
- Chang CY, Chen SJ, Tsai MF. Application of support-vector-machine-based method for feature selection and classification of thyroid nodules in ultrasound images. *Pattern Recogn* 2010;43:3494–3506.
- Chiappini F, Coilly A, Kadar H, Gual P, Tran A, Desterke C, Samuel D, Duclos-Vallee JC, Touboul D, Bertrand-Michel J, Brunelle A, Guettier C, Le Naour F. Metabolism dysregulation induces a specific lipid signature of nonalcoholic steatohepatitis in patients. *Sci Rep* 2017;7:46658.
- Chivers RC, Hill CR. A spectral approach to ultrasonic scattering from human tissue: Methods, objectives and backscattering measurements. *Phys Med Biol* 1975;20:799–815.
- D'Souza JC, Sultan LR, Hunt SJ, Schultz SM, Brice AK, Wood AKW, Sehgal CM. B-Mode ultrasound for the assessment of hepatic fibrosis: A quantitative multiparametric analysis for a radiomics approach. *Sci Rep* 2019;9:8708.
- Gramiak R, Hunter LP, Lee PPK, Lerner RM, Schenk E, Waag RC. Diffraction characterization of tissue using ultrasound. 1976 *Ultrasonics Symposium*. Annapolis, MD, USA60–63. doi: [10.1109/ULTSYM.1976.196631](https://doi.org/10.1109/ULTSYM.1976.196631).
- Han J, Kamber M, Pei J. Data mining: Concepts and techniques. San Francisco: Morgan Kaufmann; 2011. p. 113–114.
- Heymann F, Hamesch K, Weiskirchen R, Tacke F. The concanavalin A model of acute hepatitis in mice. *Lab Anim* 2015;49:12–20.
- Higuchi T, Hirata S, Yamaguchi T, Hachiya H. Liver tissue characterization for each pixel in ultrasound image using multi-Rayleigh model. *Jpn J Appl Phys* 2014;53 07KF27.
- Insana MF, Wagner RF, Brown DG, Hall TJ. Describing small-scale structure in random media using pulse-echo ultrasound. *J Acoust Soc Am* 1990;87:179–192.
- Javanaud C. The application of a fractal model to the scattering of ultrasound in biological media. *J Acoust Soc Am* 1989;86:493–496.
- Lackner C. Hepatocellular ballooning in nonalcoholic steatohepatitis: The pathologist's perspective. *Expert Rev Gastroenterol Hepatol* 2011;5:223–231.
- Liao YY, Yang KC, Lee MJ, Huang KC, Chen JD, Yeh CK. Multifeature analysis of an ultrasound quantitative diagnostic index for classifying nonalcoholic fatty liver disease. *Sci Rep* 2016;6:35083.
- Lin YH, Wan YL, Tai DI, Tseng JH, Wang CY, Tsai YW, Lin YR, Chang TY, Tsui PH. Considerations of ultrasound scanning approaches in non-alcoholic fatty liver disease assessment through acoustic structure quantification. *Ultrasound Med Biol* 2019;45: 1955–1969.
- Lizzi FL, Greenebaum M, Feleppa EJ, Elbaum M, Coleman DJ. Theoretical framework for spectrum analysis in ultrasonic tissue characterization. *J Acoust Soc Am* 1983;73:1366–1373.
- Macovski A. Medical imaging systems. Englewood Cliffs, NJ: Prentice-Hall; 1983. p. 173–203.
- Ogawa K, Fukushima M, Kubota K, Hisa N. Computer-aided diagnostic system for diffuse liver diseases with ultrasonography by neural networks. *IEEE Trans Nuclear Sci* 1998;45:3069–3074.
- Ozturk A, Grajo JR, Gee MS, Benjamin A, Zubajlo RE, Thomenius KE, Anthony BW, Samir AE, Dhyani M. Quantitative hepatic fat quantification in non-alcoholic fatty liver disease using ultrasound-based techniques: A review of literature and their diagnostic performance. *Ultrasound Med Biol* 2018;44:2461–2475.
- Parker KJ. The H-scan format for classification of ultrasound scattering. *J OMICS Radiol* 2016;5 1000236.
- Parker KJ. The first order statistics of backscatter from the fractal branching vasculature. *J Acoust Soc Am* 2019a;146:3318–3326.
- Parker KJ. Shapes and distributions of soft tissue scatterers. *Phys Med Biol* 2019b;64 175022.
- Parker KJ, Baek J. Fine-tuning the H-scan for discriminating changes in tissue scatterers. *Biomed Phys Eng Express* 2020;6 045012.
- Parker KJ, Poul SS. Burr, Lomax, Pareto, and logistic distributions from ultrasonographic speckle. *Ultrason Imaging* 2020; doi: [10.1177/0161734620930621](https://doi.org/10.1177/0161734620930621). Accessed July, 28, 2020.
- Parker KJ, Poul SS. Speckle from branching vasculature: Dependence on number density. *J Med Imaging* 2020b;7 027001.
- Parker KJ, Carroll-Nellenback JJ, Wood RW. The 3D spatial autocorrelation of the branching fractal vasculature. *Acoustics* 2019;1: 369–381.
- Peng C, Chiappini F, Kascakova S, Danulot M, Sandt C, Samuel D, Dumas P, Guettier C, Le Naour F. Vibrational signatures to discriminate liver steatosis grades. *Analyst* 2015;140:1107–1118.
- Schwen LO, Homeyer A, Schwier M, Dahmen U, Dirsch O, Schenk A, Kuepfer L, Preusser T, Schenk A. Zonated quantification of steatosis in an entire mouse liver. *Comput Biol Med* 2016;73:108–118.
- Shapiro SA. Elastic waves scattering and radiation by fractal inhomogeneity of a medium. *Geophys J Int* 1992;110:591–600.
- Sujana H, Swarnamani S, Suresh S. Application of artificial neural networks for the classification of liver lesions by image texture parameters. *Ultrason Med Biol* 1996;22:1177–1181.
- Tamura K, Mamou J, Yoshida K, Hachiya H, Yamaguchi T. Ultrasound-based lipid content quantification using double-Nakagami distribution model in rat liver steatosis. *Jpn J Appl Phys* 2020;59: SKKE23.
- Taylor HM, Ros PR. Hepatic imaging: An overview. *Radiol Clin North Am* 1998;36:237–245.
- Virmani J, Kumar V, Kalra N, Khandelwal N. PCA-SVM based CAD system for focal liver lesions using B-mode ultrasound images. *Defense Sci J* 2013a;63:478–486.
- Virmani J, Kumar V, Kalra N, Khandelwal N. SVM-based characterization of liver ultrasound images using wavelet packet texture descriptors. *J Digit Imaging* 2013b;26:530–543.
- Wu WJ, Lin SW, Moon WK. Combining support vector machine with genetic algorithm to classify ultrasound breast tumor images. *Comput Med Imaging Graphics* 2012;36:627–633.
- Yeh WC, Huang SW, Li PC. Liver fibrosis grade classification with B-mode ultrasound. *Ultrasound Med Biol* 2003;29:1229–1235.
- Zagzebski JA, Lu ZF, Yao LX. Quantitative ultrasound imaging: In vivo results in normal liver. *Ultrason Imaging* 1993;15:335–351.
- Zhou Z, Tai DI, Wan YL, Tseng JH, Lin YR, Wu S, Yang KC, Liao YY, Yeh CK, Tsui PH. Hepatic steatosis assessment with ultrasound small-window entropy imaging. *Ultrasound Med Biol* 2018;44:1327–1340.